Supplementary materials

Appendix A. Numerical solutions for solitary waves over a constant depth

In this section, the numerical model is checked with analytical solution of a solitary wave propagating over a constant depth. The free surface elevations, velocity profiles, wall shear stress on the bottom and wave height decay during propagation are all checked with theoretical results.

The solitary wave generated is 2.512 cm high and the water depth is 8.0 cm, resulting in a wave nonlinearity of $H/h = 0.314$. Thus, the effective wave length of the solitary wave is 0.964 m.

A.1. *Mesh*

The initial simulations have been performed in a quasi-three-dimensional mesh, in which the lateral direction is only discretised by one cell.

The simulation domain of 14 m long and 0.20 m high is selected so that the solitary wave propagation will not be affected by boundaries during the period of interest. Hence, comparisons between the numerical results and theoretical solutions are made at $x = 2$ m and 12 m. Given that the effective wave length of the solitary wave is close to 1 m, no reflections are expected to contaminate the data at any of these locations.

The mesh has been designed to provide an adequate cell size for wave propagation, plus an additional refinement near the bottom boundary layer for enhanced resolution. The mesh has the following characteristics: a general resolution of 1 mm in the horizontal and vertical directions along the still water level (0.08 m) ensures that the wave height is correctly discretised by more than 25 cells. Vertical cell size increases to 4 mm at the top boundary by means of a geometric progression to reduce computational cost in the air area. Finally, within the region of 2 cm above the bottom, very fine discretisation is introduced to obtain an accurate description of the bottom boundary layer. Cells in this area have a vertical size that grows from 0.1 mm to 1 mm with a geometric progression. The free surface boundary layer is considered of second order (Klettner & Eames 2012), therefore, no additional resolution is added to that area. The mesh totals 2.5 million hexahedral cells. The 15 s of simulation take 5.3 hours in 10 cores of an Intel Xeon (2.50 GHz) workstation.

A.2. *Initial and boundary conditions*

Solitary waves are generated at the left boundary, using Grimshaw's (1971) third order solitary wave solution, as referenced in Lee *et al.* (1982).

The horizontal bottom and right boundary are treated as solid walls, with no-slip boundary conditions. The top boundary is treated as an open boundary condition to the atmosphere, thus setting pressure value to atmospheric pressure.

The lateral boundaries define two parallel planes with free-slip boundary conditions. Moreover, the boundary condition indicates that the simulation is effectively 2D, eliminating the need to solve for one of the momentum equations in the normal direction to the plane (i.e. y component).

The turbulence regime has been chosen as laminar (i.e. no turbulence modelling). This is a reasonable assumption, since wave propagation under these conditions is laminar.

A.3. *Results*

The results from this simulation are presented in figure A.1. The top panel shows the evolution of the solitary wave as it travels over constant depth. It includes the numerical

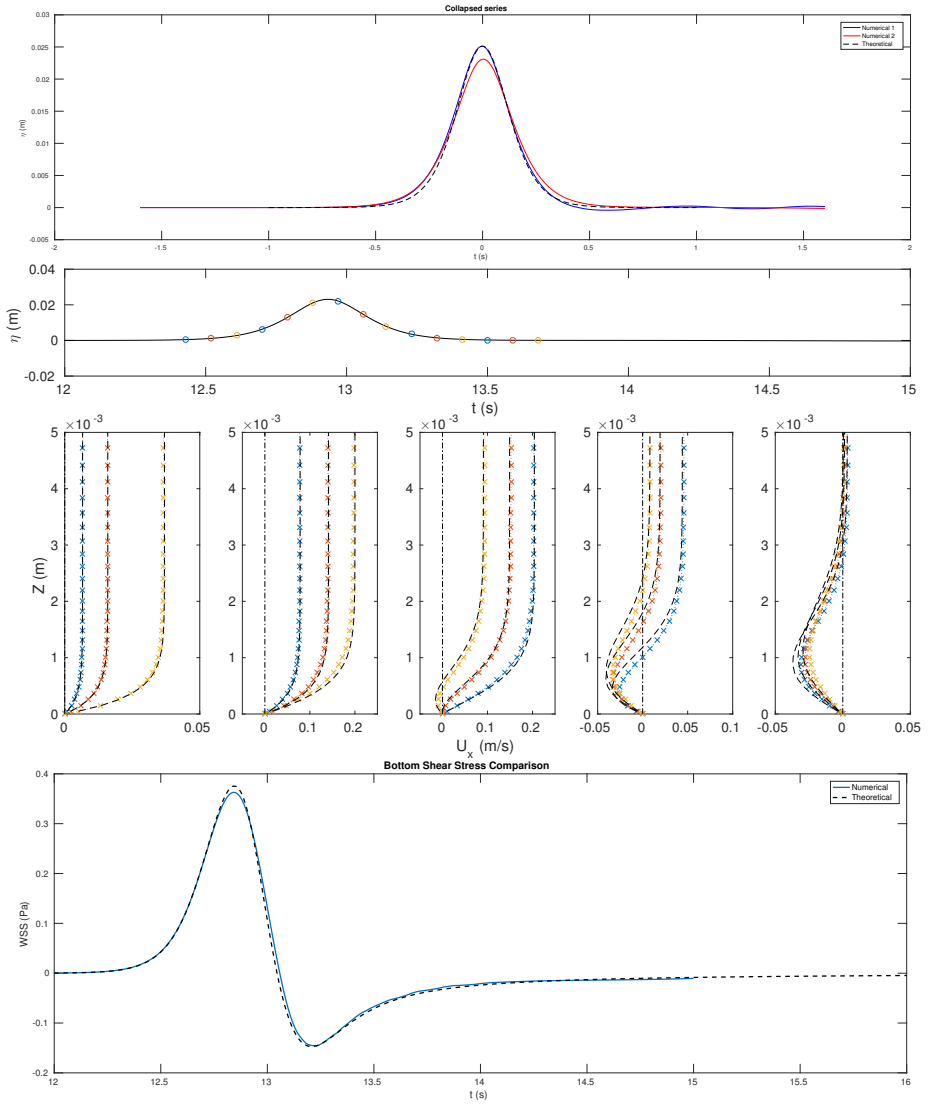

FIGURE A.1. Solitary wave propagation over a horizontal bottom. Top panel: free surface elevation at $x = 2$ m and 12 m (continuous line) and theoretical profile (dashed line). Middle panels: horizontal velocity profiles at $x = 12$ m. Sets of 3 circles mark the time sampling positions. Numerical data is presented as individual markers (one cross per cell in the mesh, the real resolution of the numerical model), theoretical data as a dashed line. Bottom panel: bottom shear stress at $x = 12$ m; numerical data as continuous line, theoretical curve in dashed line.

solutions of free surface elevations recorded at both sampling locations ($x = 2$ m and 12 m, respectively), and the analytical solution (Grimshaw 1971) using the numerically obtained wave height at $x = 2$ m.

The numerically simulated free surface profile at $x = 2$ m matches with Grimshaw's theoretical solution reasonably well. The numerical solutions show very small trailing waves, which could be caused by the imperfection in the wave generation mechanism.

After propagating 10 metres (10.37 effective wavelengths) the wave loses height and gains a more symmetric profile, thus, getting slightly longer. The trailing oscillations have also been left behind. The surface profile measurements at both wave gauges show

that the wave height decreases to 91.93% of the original value. The theoretical solution for viscous bottom boundary layer damping (Mei *et al.* 2005) suggests that the expected dissipation rate is 89.06%. Thus, the simulated wave height is slightly higher than the theoretical prediction by approximately 2%.

The middle panels of figure A.1 present the comparison of horizontal velocity profiles at 15 instants. Theoretical solutions from Liu *et al.* (2007) are also plotted for each instant. It is observed that the agreements between numerical and theoretical results are excellent during the accelerating phases. Agreement of the free stream velocity continues to be outstanding throughout the whole simulation. However, during the decelerating phases, numerical solutions tend to underestimate the theoretical solutions inside the boundary layer. It is remarked here that the magnitudes of the velocity are very small during the tail end of the wave. Discrepancies may be explained by the fact that the theoretical solution employed is only first order accurate, while nonlinearity is embedded in the equations of the numerical model.

The bottom panel in figure A.1 is a comparison of the bottom shear stress at $x = 12$ m. The theoretical value has been computed according to Liu & Orfila (2004). The numerical data has been obtained by computing the derivative at the bottom of the best-fit fourth order polynomial to the 5 closest points (vertically-adjacent cell-centres) to the ground.

The matching between the numerical solution and the theoretical expression is outstanding. However, it is noticeable that the numerical solution slightly underestimates the theoretical solution, especially at the peak instant. Again, discrepancies may be explained by the fact that the theoretical solution employed is only first order accurate, while nonlinearity is embedded in the equations of the numerical model.

These findings indicate two facts; first, the resolution of the mesh in the vicinity of the bottom is sufficient to represent meticulously the boundary layer; and second, the model accurately solves the physics involved in this setup.

Appendix B. Rundown phase velocity profile comparisons (no time and space shifting)

In this appendix we present a comparison of velocity profiles in the water column between the numerical results and the experiments for the rundown phase. Unlike in section 3.4.2, the time and space shifts are not introduced, therefore, the agreement is not as good as in the previous results. Figures B.1-B.3 correspond to figures 19-21 in the original paper.

The first instant in figure B.1 takes place at the initiation of the rundown phase. The overshoot in the numerically obtained velocity profiles progresses, getting smoother to the point of almost vanishing by $t = 0.88$ s. Also, the experimental free stream velocities progress in such a way that they start to line up again with the numerically obtained free stream velocities, closer to the toe of the slope. Large discrepancies exist further up the slope. The differences between free surface elevations also increase, especially around $x = 17$ cm, where the hydraulic jump is developing.

The panels in figure B.2 illustrate the differences of the developing hydraulic jump between the physical and numerical experiments. The maximum deviation in free surface elevation is 3.0 cm for $t = 0.96$ s. At that instant, the numerical simulation is about to reach the incipient breaking point (i.e. vertical free surface at the hydraulic jump), while the experiment still presents a gentle slope. At $t = 1.01$ s the numerical simulation is already showing the feature of wave overturning, and the experiment shows that the flow is just about to reach the incipient breaking point. Regarding velocity profiles, the degree of agreement near the toe of the slope (subcritical flow regime region) is remarkable.

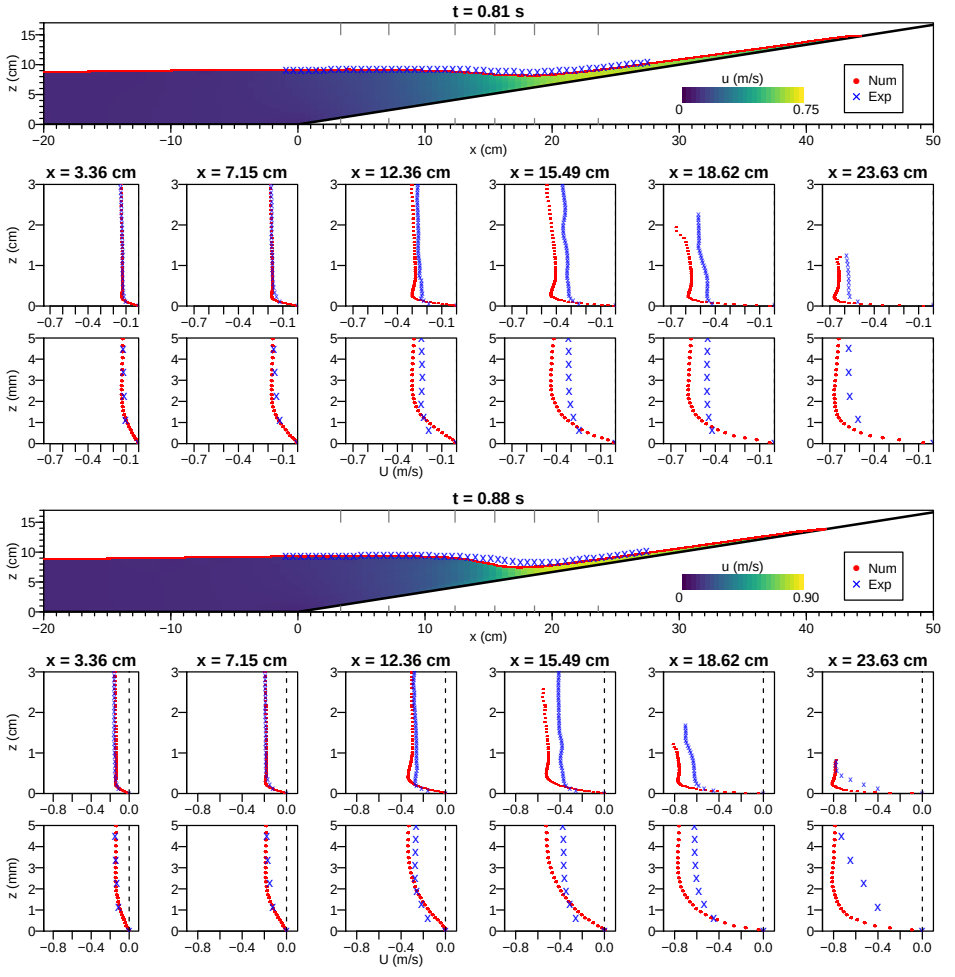

FIGURE B.1. Velocity profile comparisons during the rundown phase at $t = 0.81$ s and 0.88 s. No temporal or spatial shifts have been applied. Captions are the same as those defined in figure 16.

Closer to the hydraulic jump, similarly to what occurs for free surface, the matching between the velocities in the physical and numerical experiments is limited.

Figure B.3 shows the early breaking stage. As commented previously, the breaking timing and location are different in the experiments and in the numerical simulation. Therefore, there are also significant differences in the amount of air trapped in the system. At some locations up the slope, the rundown swash flow layer becomes so thin that the HSPIV system fails to capture velocities at the current zoom level (FOV L3, see figure 2).

Appendix C. Comparison between k-ω SST and laminar numerical simulations results

As mentioned in the main text, the thin rundown flow becomes turbulent just before onset breaking, therefore the original 3D numerical simulation was set up to use the k-ω SST turbulence model. However, since the flow remains laminar until the final stages

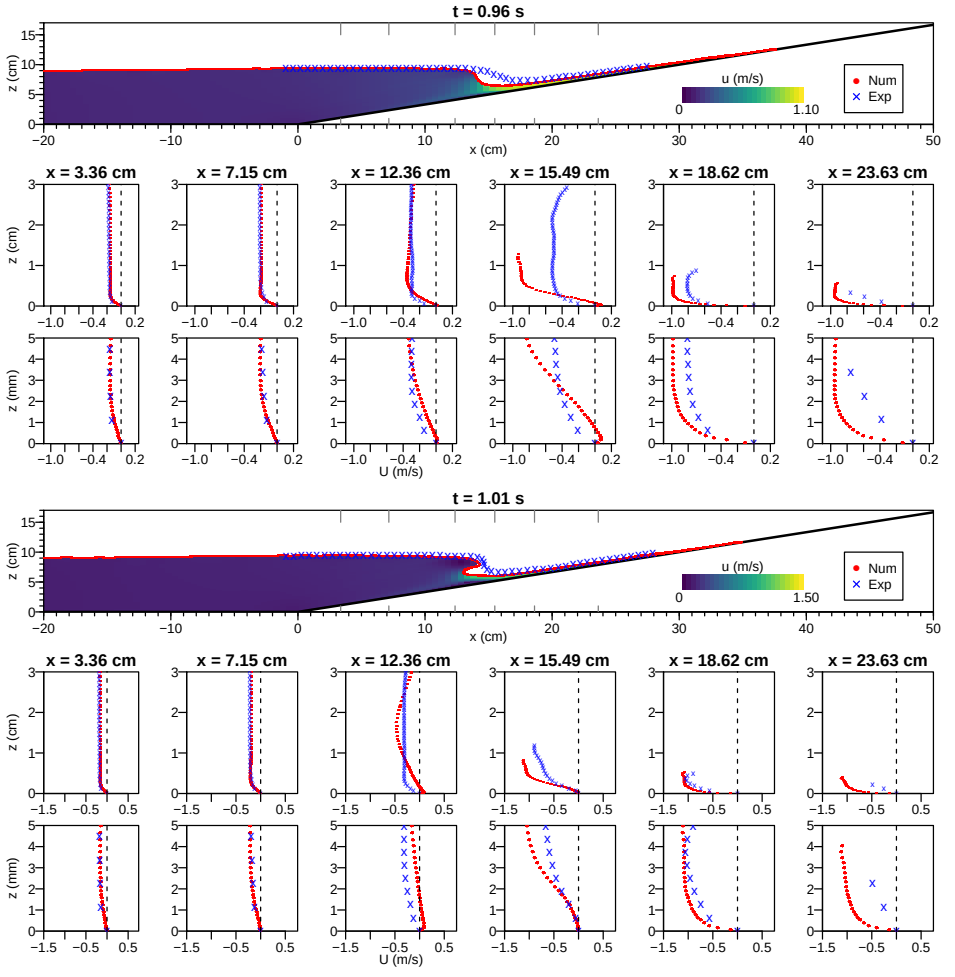

FIGURE B.2. Velocity profile comparisons during the formation of the hydraulic jump. No temporal or spatial shifts have been applied. Captions are the same as those defined in figure 16.

of the simulation, we decided to run an identical case without turbulence modelling. Nevertheless, we acknowledge that the present simulation lacks the extreme space and time discretisation required to characterize turbulence accurately as in DNS.

The differences between the present (laminar) and k-ω SST cases are virtually nonexistent prior to the hydraulic jump phase. Therefore, we will only review those results that differ significantly. The first comparison is for free surface elevation and velocity profiles in figures C.1 and C.2, which can be compared against figures 20 and 21, respectively.

Figure C.1 compares the instants just before onset breaking. Although the agreement is remarkable for both simulations there are some details that make the SST solution closer to the experimental results. First, in $x = 15.49$ cm transect (both panels) it is clear that the laminar simulation has already undergone flow reversal (onshore-directed) at the bottom, while the SST solution is just starting, thus developing a velocity profile almost identical to that in the experiment. The second feature is the overshoot in the bottom part of the downwash flow, which is milder in the SST case compared to the

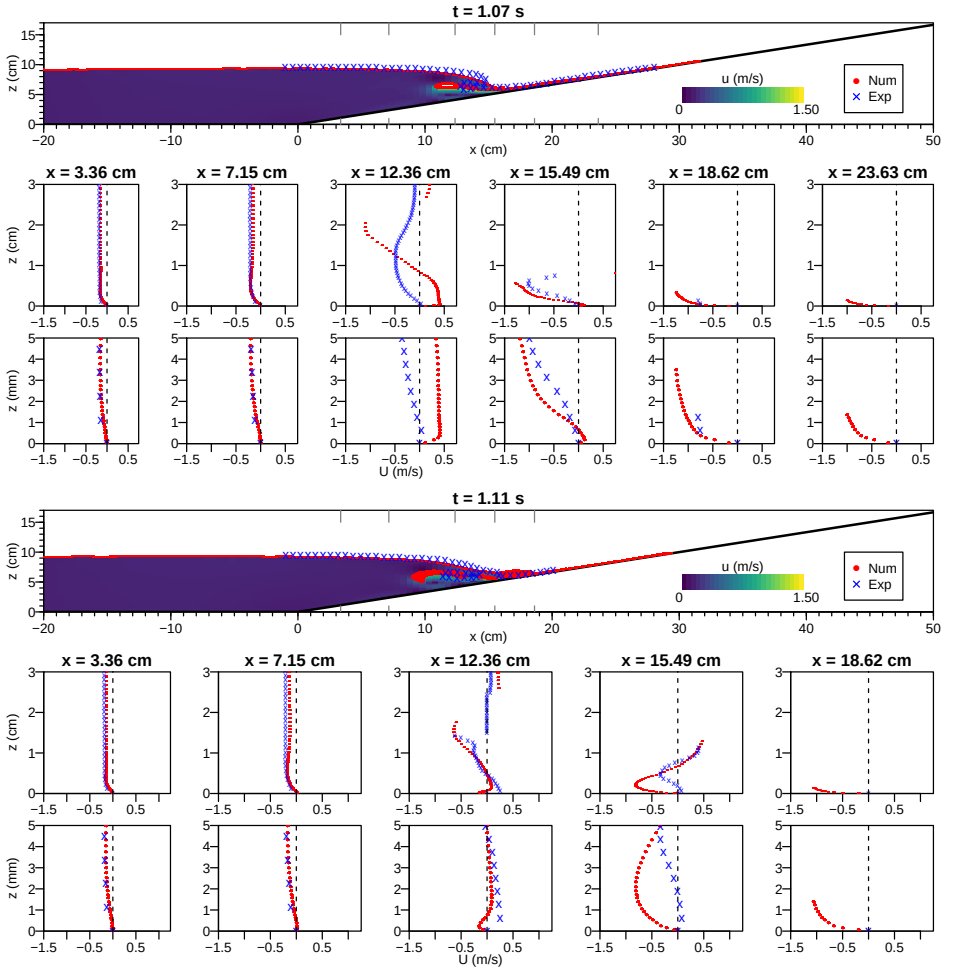

FIGURE B.3. Velocity profile comparisons during the early wave breaking stage at $t = 0.96$ s and 1.01 s. No temporal or spatial shifts have been applied. Captions are the same as those defined in figure 16.

laminar case (see $x = 15.49$ cm in the top panel), and is not evident for the experimental results.

In figure C.2, the SST results are influenced by turbulence, which increases the effective viscosity of the fluid. When compared against figure 21, the differences in free surface elevation are clear. In the SST case the local water level below the overturning wave (top panel) is higher. This discrepancy causes a significant upward shift in the position of the trapped pocket of air shortly after (bottom panel), as compared to the experiment, whereas the laminar case produces a more reasonable comparison.

Regarding velocity profiles, the laminar results present a tighter fit to the experimental data close to the bottom (top panel, $x = 12.36$ cm and $x = 15.49$ cm). The agreement above 5 mm is, in both cases, very limited. The transect $x = 12.36$ cm provides further information about the local water depth below the overturning wave. In the laminar case the free surface is located 5 mm above the level measured in the experiment, while for the SST case it is 10 mm above. Also, the vertical dimension of the vortex at that location differs. While in the laminar case the flow reversal area is 1.5 mm high (onshore-directed,

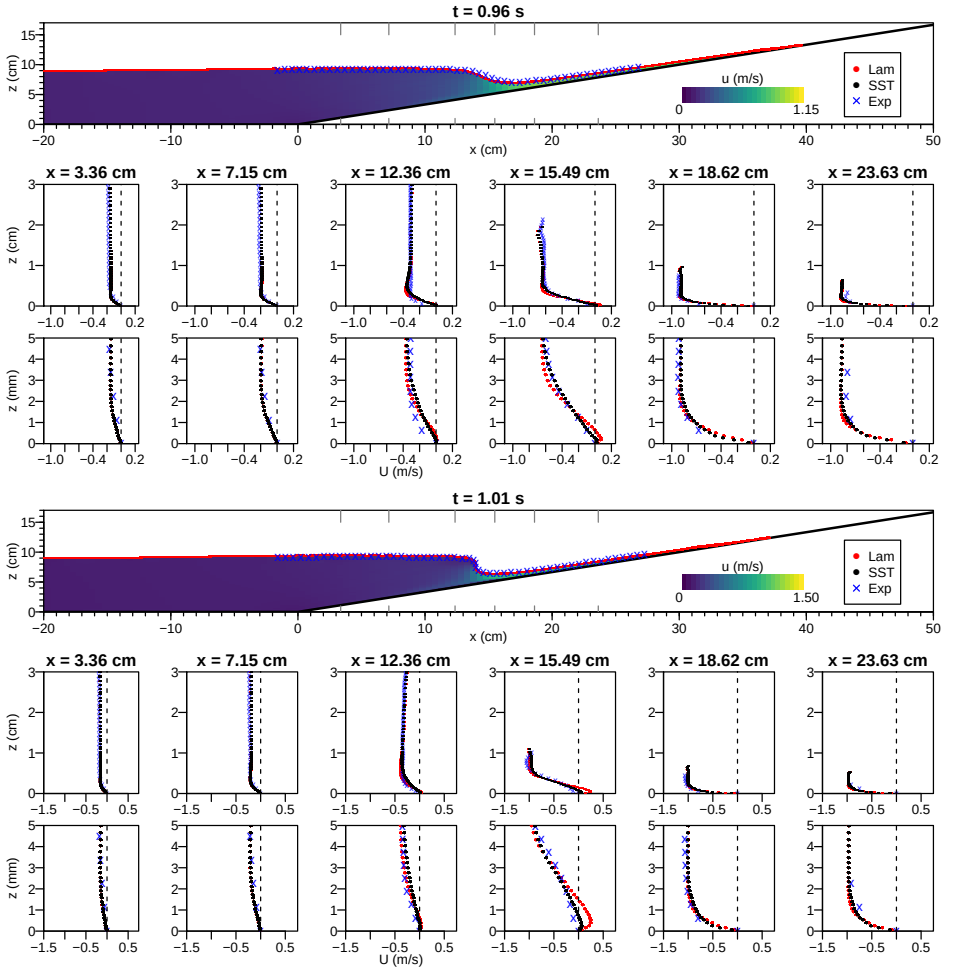

FIGURE C.1. The free surface profile and velocity field comparisons during the formation of the hydraulic jump at experimental times $t = 0.96$ s and 1.01 s, respectively. Time and space shifts have been applied. Numerical simulation times (laminar and SST) are $t = 0.92$ s and 0.97 s, respectively. Experimental results have been shifted -6.32 mm in the X direction (e.g., the profiles at $x = 3.36$ cm in the numerical simulations correspond to $x = 3.96$ cm in the experiment). Captions are the same as those defined in figure 16.

almost matching perfectly the experimental measurement), it is 7.5 mm in the SST case, almost 5 times larger. The agreement over the breaking area once wave has impacted the downwash flow ($t = 1.11$ s) is limited for both simulations.

Figure C.3 is analogous to figure 24 and displays the vortex pattern during the flow reversal and early wave breaking phases. Both figures present a strong resemblance initially ($t < 1$ s), with the main anti-clockwise vortex A being generated by a fluctuation in the horizontal pressure gradient, and growing as it is advected offshore by the downwash flow. Additional vortices, B and C, develop shortly after.

The increase of effective viscosity in the SST simulation makes the vortex A grow in the vertical direction and remain as a single block ($t = 1.01$ s in figure 24), while in the laminar simulation the vortex A stretches and develops two smaller vortices inside (A_1 and A_2, $t = 1.03$ s in figure C.3).

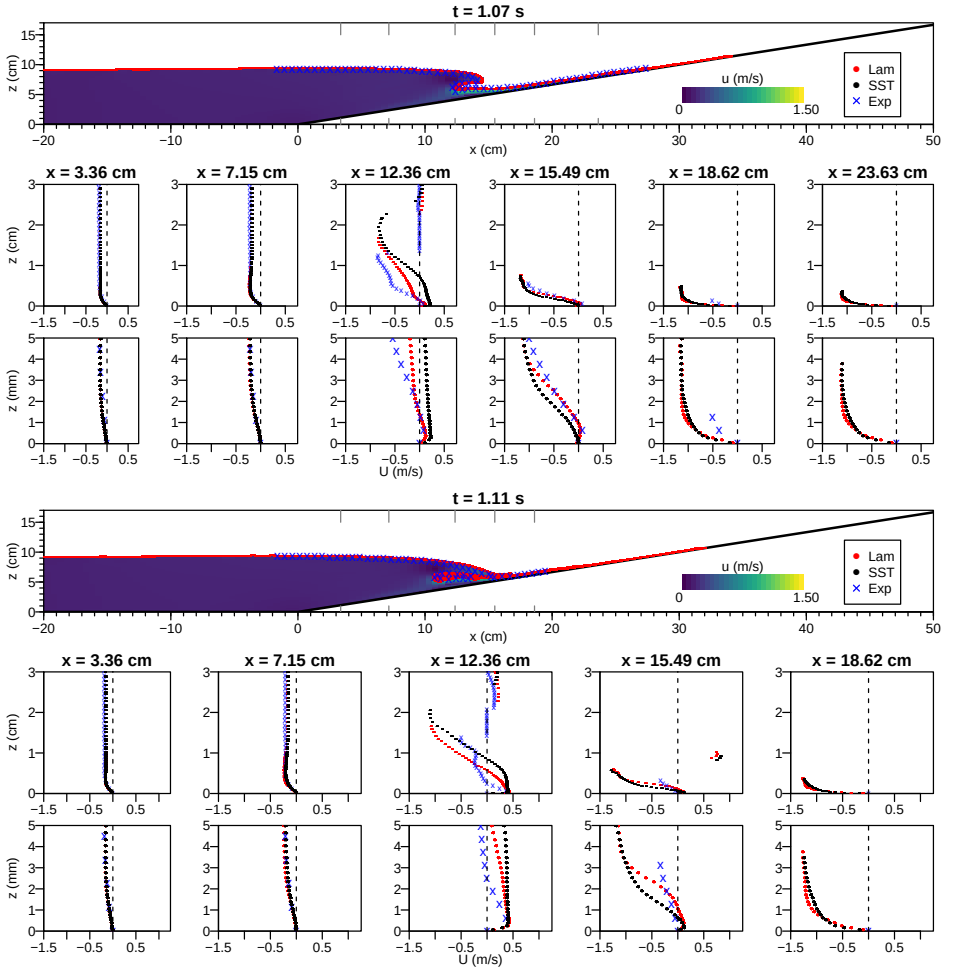

FIGURE C.2. The free surface profile and velocity field comparisons during the early wave breaking stage at experimental times $t = 1.07$ s and 1.11 s, respectively. Time and space shifts have been applied. Numerical simulation times (laminar and SST) are $t = 1.03$ s and 1.07 s, respectively. Experimental results have been shifted -6.32 mm in the X direction (e.g., the profiles at $x = 3.36$ cm in the numerical simulations correspond to $x = 3.96$ cm in the experiment). Captions are the same as those defined in figure 16.

The differences continue to grow as the wave impacts the downwash flow. As mentioned before, vortex A occupies almost the whole water depth in the SST simulation, pushing the pocket of trapped air above its expected location. Alternatively, lacking the additional viscosity, vortex A is able to further stretch downstream in the laminar solution. Furthermore, the evolution of the vortex system is different. For example, in the bottom panel in figure C.3 vortex C does not appear because it is in the process of merging with vortex A, above the clockwise vortex B.

REFERENCES

GRIMSHAW, R. 1971 The solitary wave in water of variable depth. Part 2. *Journal of Fluid Mechanics* **46**, 611–622.

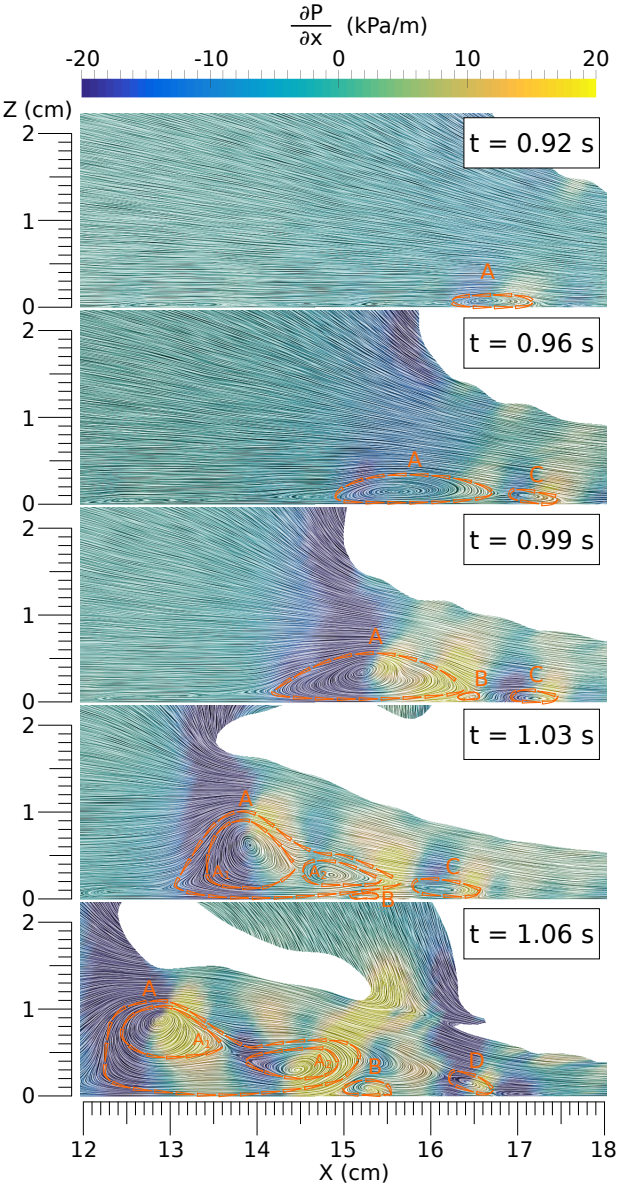

FIGURE C.3. Time evolution of vortex shedding and pressure gradient (x component) under the overturning wave visualized with the LIC technique. Laminar simulation. Vortices are marked with triangles, indicating the direction of rotation, and tagged with letters.

KLETTNER, C. A. & EAMES, I. 2012 The laminar free surface boundary layer of a solitary wave. *Journal of Fluid Mechanics* **696**, 423–433.

LEE, J. J., SKJELBREIA, E. & RAICHLEN, F. 1982 Measurement of velocities in solitary waves. *Journal of Waterway, Port, Coastal and Ocean Engineering* **108**, 200–218.

LIU, P. L.-F. & ORFILA, A. 2004 Viscous effects on transient long-wave propagation. *Journal of Fluid Mechanics* **520**, 83–92.

LIU, P. L.-F., PARK, Y.-S. & COWEN, E. A. 2007 Boundary layer flow and bed shear stress under a solitary wave. *Journal of Fluid Mechanics* **574**, 449–463.

MEI, C. C., STIASSNIE, M. & YUE, D. K.-P. 2005 *Theory and applications of ocean surface waves.*, *Advanced Series on Ocean Engineering*, vol. 23. World Scientific, Singapore.